IEEE Access
Multidisciplinary ⋮ Rapid Review ⋮ Open Access Journal

Received 17 June 2026, accepted 17 July 2026, date of publication 22 July 2026, date of current version 30 July 2026.

Digital Object Identifier 10.1109/ACCESS.2026.3716091

RESEARCH ARTICLE

An OPF-Based Control Framework for Hybrid AC–MTDC Power Systems Under Uncertainty

HONGJIN DU, (Graduate Student Member, IEEE), **RAHUL RANE**, (Student Member, IEEE), **WEIJIE XIA**, (Student Member, IEEE), **PEDRO P. VERGARA**, (Senior Member, IEEE), **AND ALEKSANDRA LEKIĆ**, (Senior Member, IEEE)

Department of Electrical Sustainable Energy, Delft University of Technology, 2628 CD Delft, The Netherlands

Corresponding author: Hongjin Du (h.du@tudelft.nl)

This work was supported in part by China Scholarship Council (CSC) and in part by CRESYM Project Harmony.

ABSTRACT The increasing integration of renewable energy, particularly offshore wind, introduces significant uncertainty into hybrid AC–HVDC systems due to forecast errors and power fluctuations. Conventional control strategies typically rely on fixed setpoints and neglect frequency deviations, which compromise system stability under rapid renewable variations. To address the challenge, this paper presents an optimal power flow (OPF)–based adaptive control framework for hybrid AC–MTDC systems with offshore wind integration. To enable the time-coupled OPF to produce anticipatory setpoints under wind variability, a Random Forest–based wind-speed forecast is integrated as an uncertainty-aware data source, providing the OPF with an informed view of the wind trajectory over the dispatch horizon. The resulting baseline setpoints are further adjusted in real time through an adaptive droop control scheme that simultaneously regulates DC voltage and AC frequency to enhance robustness across a broad class of disturbances. The effectiveness of the proposed framework is validated through hardware-in-the-loop simulations against three benchmark control modes, demonstrating consistent and balanced performance under wind-forecast uncertainty, AC-side load steps, and DC-side faults.

INDEX TERMS Droop control, VSC–MTDC, optimal power flow, wind forecast.

I. INTRODUCTION

In recent years, the global energy landscape has been undergoing a steady transformation driven by the increasing adoption of renewable energy sources (RESs). Recent analyses, such as Ember's Global Electricity Review 2025 [1], indicate that renewable energy has been playing an increasingly prominent role in global electricity generation over the past decade. Nevertheless, integrating high shares of RESs into large-scale power systems remains a significant technical and operational challenge [2].

High voltage direct current (HVDC) technology has been widely adopted as an efficient means of long-distance power transmission and renewable energy integration [3]. Among different technologies, voltage source converter (VSC)–based HVDC, especially with modular multilevel converters (MMCs), has gained prominence due to its advanced controllability. Unlike traditional line-commutated converters (LCCs), VSCs can independently control active and reactive power, operate in weak or even passive grids, and support multi-terminal or meshed configurations. These features make VSCs particularly suitable for hybrid AC–HVDC power systems dominated by renewable energy. With the maturation of VSC—HVDC technology, the key challenge lies not in its technical feasibility but in ensuring secure and coordinated operation under various operating conditions, such as wind forecast uncertainties and grid disturbances [4].

In practice, these challenges are exacerbated by the intermittency and unpredictability of wind generation, which introduces power mismatches and additional operating costs in day-ahead and balancing markets [5]. The interaction between uncertain wind generation and the dynamics of DC systems further increases operational complexity.

The associate editor coordinating the review of this manuscript and approving it for publication was Fabio Mottola.

Existing studies often address these mismatches by computing optimal operating points with stochastic or probabilistic optimal power flow (OPF) [6], [7]. Although these approaches capture uncertainty better than deterministic models, they impose high computational burdens and scale poorly, limiting their use in large-scale, real-time operation.

While OPF yields economically efficient and coordinated operating points [8], the fixed setpoints produced are not well suited to dynamic conditions, as they cannot adapt to disturbances or forecast errors, potentially resulting in degraded performance or even oscillatory behavior. Consequently, these steady-state setpoints must be complemented by closed-loop real-time control to continuously reject fast transients and accurately track the optimal trajectory.

Conventional voltage control strategies include master–slave control, which enables accurate power sharing but depends on fast and reliable communication, and voltage droop control, which operates solely based on local voltage and current measurements. By eliminating the need for extensive communication, droop control inherently facilitates decentralized operation and improves system scalability, making it the preferred approach for complex multi-terminal HVDC (MTDC) systems [9], [10].

Nevertheless, fixed droop gains may result in uneven power sharing, which can lead to converter overloads or underutilization [11]. To overcome these limitations, adaptive and nonlinear droop control methods have been proposed in [12], [13], [14], [15], [16], and [17]. For instance, the power headroom (i.e., the difference between the rated capacity and the present loading) was introduced to improve power sharing [12], but DC-voltage deviation under both transient and steady-state conditions was not considered. In [13], an adaptive droop strategy addressing both power sharing and DC-voltage deviation was proposed; however, it neglects frequency dynamics, which are essential for coordinated AC–DC operation. More broadly, most existing control strategies for VSC-MTDC systems are developed under the assumption of constant frequency. Consequently, conventional droop strategies are designed almost exclusively for DC-voltage regulation, neglecting the inherent coupling between DC variables and AC frequency, as well as the influence of power injections at the point of common coupling (PCC) on overall system dynamics.

To address these limitations, this paper proposes an OPF-based adaptive control framework for AC–MTDC systems under high renewable penetration. The main contributions of this work are as follows:

1) *Vertical closed-loop integration of the forecasting, scheduling, and real-time droop layers.* A Random Forest (RF) wind-speed forecaster drives a time-coupled OPF to generate anticipatory dispatch setpoints. These setpoints establish the baseline for the real-time droop layer, whose adaptive coefficients are explicitly parameterized by the OPF-derived operating margins. This vertical coupling effectively bridges the macroscopic scheduling and microsecond-level control domains, representing a structural synergy missing in either literature stream considered separately.
2) *A droop law that co-regulates AC frequency alongside DC voltage.* The active-power reference of each onshore converter is augmented with coupled DC-voltage and AC-frequency feedback terms, utilizing margin-aware coefficients that continuously adapt to the available converter headroom. This formulation enables the converter to dynamically reallocate its capacity between voltage and frequency support based on the specific disturbance type, providing a critical resilience inherently lacking in conventional voltage-only droop schemes.
3) *Hardware-in-the-loop (HIL) validation of the proposed framework on a AC–MTDC test system.* The experimental validation isolates the steady-state economic benefits of the forecast-integration step via a persistence-baseline comparison, and rigorously extracts quantitative dynamic-response indices to benchmark the adaptive droop layer against three conventional control strategies.

The remainder of this paper is organized as follows. Section II presents the system modeling and problem formulation. Section III introduces the proposed forecast-integrated OPF and adaptive droop control framework. The feasibility of the proposed control scheme and its transient performance are evaluated through simulations in Section IV, and Section V concludes the paper and outlines directions for future research.

II. AC–MTDC SYSTEM MODELING AND OPTIMAL POWER FLOW

The hybrid AC–MTDC system investigated in this work comprises multiple AC areas interconnected via a VSC–MTDC grid. The comprehensive analytical model integrates detailed formulations of the AC and DC networks, the converter stations, and the underlying OPF framework that governs the coordinated operation analysis [18].

A. AC SYSTEM MODELLING

The AC subgrid is represented by steady-state nodal power flow equations that describe the active and reactive power injections at each bus. For each bus $i \in \mathcal{N}_{\mathrm{ac}}$, the injected powers can be expressed as:

$$P_i = U_i \sum_{j=1}^{n} U_j \left[G_{ij}\cos(\delta_i - \delta_j) + B_{ij}\sin(\delta_i - \delta_j)\right], \quad (1)$$

$$Q_i = U_i \sum_{j=1}^{n} U_j \left[G_{ij}\sin(\delta_i - \delta_j) - B_{ij}\cos(\delta_i - \delta_j)\right], \quad (2)$$

where U_i and U_j are the voltage magnitudes at buses i and j, δ_i and δ_j are their corresponding voltage phase angles, and G_{ij} and B_{ij} denote the conductance and susceptance elements of the network admittance matrix, respectively.

Correspondingly, the nodal active and reactive power balances are enforced as:

$$P_{G,i} - P_{D,i} - P_i = 0, \quad Q_{G,i} - Q_{D,i} - Q_i = 0, \tag{3}$$

where $P_{G,i}$ and $Q_{G,i}$ represent the active and reactive power generation, and $P_{D,i}$ and $Q_{D,i}$ denote the corresponding power demands.

Conventional generators are constrained by their operational limits:

$$P_{G,i}^{\min} \le P_{G,i} \le P_{G,i}^{\max}, \quad Q_{G,i}^{\min} \le Q_{G,i} \le Q_{G,i}^{\max}. \tag{4}$$

Furthermore, the voltage magnitude and phase angle at each bus are bounded by their operational limits:

$$U_i^{\min} \le U_i \le U_i^{\max}, \quad \delta_i^{\min} \le \delta_i \le \delta_i^{\max}. \tag{5}$$

Converter stations are connected at specific AC buses, where their active and reactive power injections are incorporated as additional terms in (3). These coupling points establish the critical interface between the AC and DC subgrids, facilitating coordinated optimization and control across the integrated system.

B. DC SYSTEM MODELLING

The DC subgrid is represented by nodal current balance equations that describe the relationship between DC voltages and line currents. For each DC bus $m \in \mathcal{N}_{dc}$, the injected current can be expressed as:

$$I_{dc,m} = \sum_{n=1,n\neq m}^{N_{dc}} Y_{dc,mn}(U_{dc,m} - U_{dc,n}), \tag{6}$$

where $U_{dc,m}$ and $U_{dc,n}$ denote the DC voltage magnitudes at buses m and n, respectively, and $Y_{dc,mn}$ is the DC network admittance between them.

The injected DC power at bus m is given by:

$$P_{dc,m} = U_{dc,m} I_{dc,m}, \tag{7}$$

where $P_{dc,m}$ denotes the DC-side power of the VSC connected at bus m, with positive values indicating power injection into the DC grid and negative values indicating power withdrawal.

To ensure safe operation of the converters, the DC power at each terminal is constrained by its rated limits:

$$P_{dc,m}^{\min} \le P_{dc,m} \le P_{dc,m}^{\max}. \tag{8}$$

C. VSC CONVERTER MODELLING

The active power loss of converter station k, denoted by $P_{loss,k}$, comprises three distinct components: a constant no-load loss, a linear conduction loss, and a quadratic loss. The total loss is thus formulated as a second-order polynomial of the AC-side reactor current $I_{c,k}$:

$$P_{loss,k} = a + bI_{c,k} + cI_{c,k}^2, \tag{9}$$

$$P_{c,k}^2 + Q_{c,k}^2 = 3U_{c,k}^2 I_{c,k}^2, \tag{10}$$

TABLE 1. VSC loss coefficients.

	a [MW]	b [kV]	c [Ω]
VSC 1 and 4	0.3183	1.4256	0.2049
VSC 2 and 3	0.1769	0.8594	0.3155

where $P_{c,k}$ and $Q_{c,k}$ denote the active and reactive power at the converter AC terminal, and $U_{c,k}$ is the AC-side voltage magnitude of converter k. This station-level representation is a well-established formulation for VSC losses in steady-state power flow studies of AC–HVDC systems [18], [19], [20]. It preserves the dominant physical loss mechanisms while remaining differentiable and computationally tractable for interior-point OPF solvers.

The loss coefficients a, b, and c are identified through a systematic curve-fitting procedure. Specifically, the converter is evaluated across its rated power range using a high-fidelity, switching-level model. At each operating level, the total power loss is quantified as the mismatch between the measured AC- and DC-side powers, recorded alongside the corresponding reactor current $I_{c,k}$. Subsequently, a second-order polynomial of the form (9) is fitted to these empirical loss–current pairs via least squares regression.

The same procedure applies without modification to any converter rating or system configuration, and only the resulting values of a, b, and c change. As a qualitative guideline, the constant term a scales with the converter's standby loss, the linear term b with the IGBT conduction voltage drop, and the quadratic term c with the on-state and copper resistances, but the relative weighting of the three terms depends on the submodule topology and switching frequency and must therefore be re-identified for each new converter. The coefficients reported in Table 1 correspond to this procedure applied to the converter model employed in this study.

In addition to the loss model in (9)–(10), each converter station $k \in \mathcal{N}_c$ is subject to a set of operational constraints that jointly define its feasible operating region within the OPF formulation:

$$0 \le I_{c,k} \le I_{c,k}^{\max}, \tag{11a}$$

$$U_{c,k}^{\min} \le U_{c,k} \le U_{c,k}^{\max}, \tag{11b}$$

$$P_{c,k}^{\min} \le P_{c,k} \le P_{c,k}^{\max}, \tag{11c}$$

$$Q_{c,k}^{\min} \le Q_{c,k} \le Q_{c,k}^{\max}, \tag{11d}$$

$$P_{c,k}^2 + Q_{c,k}^2 \le \left(S_{c,k}^{\max}\right)^2, \tag{11e}$$

$$U_{dc,k}^{\min} \le U_{dc,k} \le U_{dc,k}^{\max}. \tag{11f}$$

where $I_{c,k}^{\max}$ denotes the rated reactor current of converter k; $U_{c,k}^{\min}$ and $U_{c,k}^{\max}$ define the admissible range of the converter AC-side terminal voltage required for valid modulation; $P_{c,k}^{\min}$, $P_{c,k}^{\max}$, $Q_{c,k}^{\min}$, and $Q_{c,k}^{\max}$ are the lower and upper bounds on the active and reactive power exchanged at the converter AC terminal; $S_{c,k}^{\max}$ is the apparent-power rating of converter k, which together with (11e) enforces the converter's PQ-capability curve; and $U_{dc,k}^{\min}$ and $U_{dc,k}^{\max}$ are the lower and upper bounds on the DC-side terminal voltage of the bus to which converter k is connected. The DC-voltage bound (11f) complements the DC-side power limit already stated in (8) and ensures safe DC-side operation under all admissible operating conditions.

D. OPTIMAL POWER FLOW FORMULATION

The optimal operating point of the system is obtained by solving the following OPF problem, which minimizes total generation cost subject to AC, DC, and converter constraints. The decision variables are collected in the vector x, comprising the active-power generation, AC-bus voltage magnitudes and angles, DC-node voltages, and VSC control variables:

$$\begin{aligned} \min_{x} \quad & f(x) = \sum_{i \in \mathcal{G}} C_i(P_{\mathrm{G},i}) \\ \text{s.t.} \quad & \text{AC grid constraints (Section II-A)}, \\ & \text{DC grid constraints (Section II-B)}, \\ & \text{VSC converter constraints (Section II-C)} \end{aligned} \tag{12}$$

The generation cost of each generator is represented by a quadratic function:

$$C_i(P_{\mathrm{G},i}) = \alpha_i P_{\mathrm{G},i}^2 + \beta_i P_{\mathrm{G},i} + \gamma_i, \tag{13}$$

where α_i, β_i, and γ_i are the cost coefficients corresponding to generator $i \in \mathcal{G}$. The quadratic cost function in (13) conventionally models the operating costs of thermal generators. It is the default cost formulation adopted by both the IEEE benchmark systems and the AC–MTDC OPF framework in [20]. The resulting setpoints establish the deterministic baseline for the forecast-integrated control framework detailed in Section III.

We note that the OPF formulation in (12) is deterministic and is solved for a single-point forecast of the wind trajectory, rather than through complex stochastic or robust formulations that embed the wind distribution within the optimization. This carries a clear limitation. Because only the forecasted realization enters the objective and constraints, the computed setpoints are optimal at the forecast point but offer no explicit probabilistic guarantee of cost optimality or constraint satisfaction once the realized wind deviates, and no operating reserve is co-optimized against the uncertainty set. Under large or systematically biased forecast errors, the scheduled operating point can drift from the true optimum, leaving a correspondingly larger correction to be absorbed downstream. This is a deliberate architectural choice: the burden of handling forecast uncertainty is delegated to the real-time droop layer of Section III-C rather than encoded at the OPF layer, which preserves the computational tractability of the standard AC–MTDC OPF while relying on the margin-scaled droop law for closed-loop robustness against forecast errors.

III. FORECAST-INTEGRATED OPF–BASED CONTROL FRAMEWORK

The effectiveness of OPF formulations under high RES penetration hinges on the accurate anticipation of wind trajectories. To address this, the proposed OPF framework incorporates a dedicated forecasting module, utilizing an RF model to map historical data to future wind-speed profiles [21], [22]. By leveraging established forecasting methodologies, this data-driven component provides a realistic, uncertainty-aware data stream that enables the time-coupled OPF to generate anticipatory setpoints under wind variability.

A. RANDOM FOREST MODEL FOR WIND SPEED FORECASTING

Driven by the multi-timescale nature of the integrated system, an RF model is selected as the forecasting engine. Operating at an hour-ahead resolution, this forecasting loop is several orders of magnitude slower than dynamic droop control. Consequently, per-inference latency is not a binding constraint, allowing the framework to prioritize modeling robustness over execution speed. The RF ensemble is therefore employed for its inherent tolerance to non-linear wind dynamics and feature noise, yielding a highly reproducible baseline with minimal hyperparameter tuning.

With the model and its operating scope established, the forecasting task is cast as a supervised multi-output regression problem, in which a single model maps a window of past observations to several future steps. The training dataset is defined as:

$$\mathcal{D} = \big\{ (X_i, Y_i) \, \big| \, i = 1, 2, \ldots, N \big\}, \tag{14}$$

where $X_i \in \mathbb{R}^d$ is the input feature vector and $Y_i \in \mathbb{R}^P$ is the output vector of future wind speed values.

A RF regressor is used and constructs an ensemble of T decision trees $\{f_t(\cdot)\}_{t=1}^{T}$, each trained on a bootstrap sample of $\mathcal{D}$ [23]. For each tree, a subset of features is randomly selected at each split, ensuring diversity across the ensemble.

The prediction of a single tree is given by

$$\hat{Y}_i^{(t)} = f_t(X_i), \quad f_t : \mathbb{R}^d \to \mathbb{R}^P, \tag{15}$$

and the RF prediction is obtained by averaging over all trees

$$\hat{Y}_i = \frac{1}{T} \sum_{t=1}^{T} \hat{Y}_i^{(t)}. \tag{16}$$

Thus, the RF estimator can be written as

$$\hat{f}(X) = \frac{1}{T} \sum_{t=1}^{T} f_t(X), \tag{17}$$

where $\hat{f} : \mathbb{R}^d \to \mathbb{R}^P$ denotes the ensemble predictor.

The dataset used in this study is provided by the IEEE DataPort "Hybrid Energy Forecasting and Trading Competition" [24], in which wind observations are recorded at a native temporal resolution of 30 minutes per time step. Accordingly, the historical window $H = 48$ corresponds to 24 hours of past observations, and the prediction horizon $P = 24$ corresponds to 12 hours ahead, which matches one full diurnal cycle of wind-speed variability and a typical intra-day rolling-dispatch interval used in OPF-based scheduling, respectively. Although the original dataset spans

September 2020 to October 2023, only the first 20,000 time steps (September 2020 to January 2022, approximately 13.7 months) are used in this work. The dataset is partitioned chronologically into training, validation, and test subsets at a ratio of 60 % / 10 % / 30 %, ensuring that the test set consists entirely of observations strictly posterior to the training and validation windows and thereby avoiding temporal leakage.

Consequently, the number of trees is set to $T = 15$. This value was set through a preliminary empirical exploration rather than by default. During development, the RF forecaster was trained for several values of T over a representative range ($T \in [10, 50]$) and evaluated by its validation error on the held-out subset of the selected dataset. Consistent with the well-established convergence behavior of tree ensembles, the validation error decreased rapidly up to $T \approx 15$ and then saturated, with further increases yielding only marginal improvements (below 1 % in mean absolute error (MAE)) at the cost of substantially higher training time and memory footprint. $T = 15$ was therefore selected as an empirically validated balance between predictive accuracy and computational economy. This choice is also consistent with the input feature dimensionality of 98 used in this work and with the range commonly reported in RF-based wind-forecasting studies [22], [25]. Beyond the number of trees, no further hyperparameter tuning was performed: the maximum tree depth was left unlimited, the minimum number of samples required to split an internal node was set to 2, the minimum number of samples per leaf was set to 1, and the number of features considered at each split was set to $\sqrt{d}$, where d is the input feature dimensionality.

The forecasting model input combines historical wind-related variables and temporal features. Specifically, the last 48 time steps of wind power output and wind speed, together with the hour of the day encoded via sine and cosine transformations, are concatenated into a feature vector. The model outputs forecasts for the next 24 time steps, formulating a supervised multi-output regression task that maps the historical window to the future wind trajectory. Formally, given a history window of length $H = 48$, the input vector is defined as:

$$X_t = [\, y_{t-H}, \ldots, y_{t-1},\ s_{t-H}, \ldots, s_{t-1}, \sin\left(\frac{2\pi h_t}{24}\right),\ \cos\left(\frac{2\pi h_t}{24}\right) \Big] \tag{18}$$

where y denotes wind output, s denotes wind speed, and h_t is the hour of day at time t. The corresponding output is the sequence of future wind speeds

$$Y_t = \left[s_t, s_{t+1}, \ldots, s_{t+P-1}\right], \tag{19}$$

where $P = 24$ represents the prediction horizon.

The RF model is trained on these input–output pairs. During inference, the trained model generates predictions $\hat{Y}_t$ for unseen test samples, thereby providing a 24-step-ahead wind speed forecast. Figure 1 illustrates the comparison between the observed and predicted wind speeds using the RF model. The results demonstrate that the model effectively

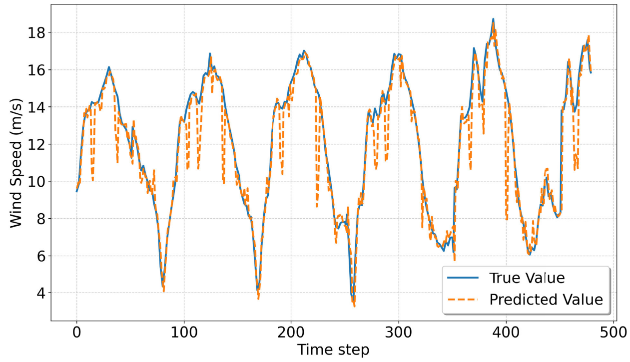

FIGURE 1. Wind speed prediction results.

reproduces the temporal dynamics of wind speed, achieving an MAE of 0.1439 m/s and a root mean square error (RMSE) of 0.6448 m/s on the test set, where the larger RMSE reflects occasional large errors at wind-ramp events. The repeated dips visible in Figure 1 at approximately the same time each day reflect the well-known diurnal pattern of near-surface wind speed: due to diurnal boundary-layer mixing driven by the daily cycle of solar heating and radiative cooling, surface wind speeds typically reach a minimum in the late-night/early-morning hours and recover during the afternoon. This periodicity is captured in the proposed feature representation through the sine and cosine hour-of-day encodings in (18), which is why the predicted trajectory in Figure 1 reproduces the daily dips.

By feeding the predicted wind speeds into the OPF, the framework updates the converter setpoints in anticipation of wind fluctuations rather than reacting to them after they occur. The residual mismatch between the forecast and the realized wind is then absorbed by the real-time droop layer described in Section III-B.

B. ADAPTIVE DROOP CONTROL STRATEGY

While the forecasting layer establishes the baseline operating point, the droop layer described here governs the converters' real-time response. To this end, the adaptive droop law co-regulates DC voltage and AC frequency by augmenting the active-power reference of each converter. For converter k, the reference is defined as:

$$P_{c,k} = P_{c,ref} + \Delta P_{v,k} - \Delta P_{f,k}, \tag{20}$$

where $\Delta P_{v,k}$ and $\Delta P_{f,k}$ represent the active power adjustments associated with DC voltage and AC frequency regulation at converter k, respectively.

The voltage-related adjustment is expressed as:

$$\Delta P_{v,k} = \frac{U_{dc,ref} - U_{dc,k}}{k_{v,k}}, \tag{21}$$

and the frequency-related adjustment is defined by:

$$\Delta P_{f,k} = \frac{f_{k,ref} - f_k}{k_{f,k}}, \tag{22}$$

where $k_{v,k}$ and $k_{f,k}$ are the voltage and frequency droop coefficients, respectively. These coefficients determine the converter's sensitivity to local DC voltage and frequency deviations.

The droop coefficients are determined by the converter's available power margin and the corresponding operating range. The voltage droop coefficient is given by:

$$k_{v,k} = \frac{U_{dc,k}^{max} - |U_{dc,ref} - 1|}{\alpha_v (P_k^{max} - |P_k|)}, \tag{23}$$

and the frequency droop coefficient by:

$$k_{f,k} = \frac{\Delta f_k^{max}}{\alpha_f (P_k^{max} - |P_k|)}, \tag{24}$$

where the Δf_k^{max} is the maximum allowable frequency deviation. α_v and α_f are tunable sensitivity parameters introduced to dynamically adjust the converter's contribution to voltage and frequency regulation. We adopt the normalization

$$\alpha_v + \alpha_f = 1, \tag{25}$$

which fully distributes the available margin between the two channels. The limiting cases $\alpha_v = 1$ and $\alpha_v = 0$ reduce the proposed scheme to pure voltage droop and pure frequency droop, respectively, so the operating region of interest is $\alpha_v \in (0, 1)$. In this work, $\alpha_v = 0.8$ and $\alpha_f = 0.2$ are adopted.

Substituting (23)–(24) into (21) and (22) yields the closed-form expressions

$$\Delta P_{v,k} = \alpha_v \left(P_k^{max} - |P_k|\right) \frac{U_{dc,ref} - U_{dc,k}}{U_{dc,k}^{max} - |U_{dc,ref} - 1|}, \tag{26}$$

$$\Delta P_{f,k} = \alpha_f \left(P_k^{max} - |P_k|\right) \frac{f_{k,ref} - f_k}{\Delta f_k^{max}}, \tag{27}$$

which expose the coupling between the DC-voltage and AC-frequency regulation channels at three levels. Locally, the two adjustments share the same available active-power margin ($P_k^{max} - |P_k|$), so that α_v and α_f act as a reserve-allocation policy between the two channels.

At the system level, DC voltage and AC frequency are physically coupled through the converter's active power even in the absence of explicit cross-channel control. An AC-side disturbance modulates the DC-side power balance via the HVDC link, and a DC-side disturbance modulates the AC-side frequency through the corresponding adjustment of the converter's PCC injection.

At the control level, the ratio

$$\frac{\Delta P_{v,k}}{\Delta P_{f,k}} = \frac{\alpha_v}{\alpha_f} \cdot \frac{(U_{dc,ref} - U_{dc,k})/(U_{dc,k}^{max} - |U_{dc,ref} - 1|)}{(f_{k,ref} - f_k)/\Delta f_k^{max}} \tag{28}$$

shows that the converter's power-allocation decision is governed by the relative (i.e., safe-band-normalized) voltage and frequency errors weighted by α_v/α_f: when the relative DC-voltage error dominates, the controller commits more of its margin to voltage support, and conversely when the relative frequency error dominates, without any explicit mode-switching logic.

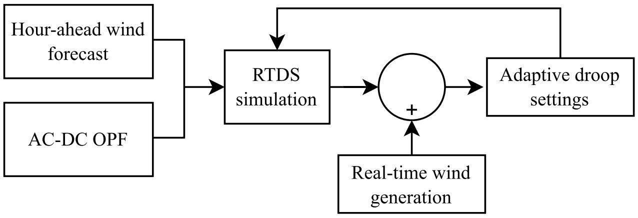

FIGURE 2. Flowchart of the proposed control strategy.

This margin-aware formulation also clarifies how forecast errors propagate from the forecasting module to real-time control. Because the droop coefficients in (23)–(24) scale with the available converter power margin, the controller allocates reserve to voltage and frequency regulation in proportion to the headroom that remains as the operating point drifts from the OPF setpoint under forecast error. The resilience of the closed loop is thereby decoupled from the pointwise accuracy of the forecast, as confirmed empirically by the persistence-baseline comparison in Scenario 1 of Section IV.

C. OVERALL CONTROL FRAMEWORK

The proposed framework couples the forecasting and OPF layers of Sections III-A and III-B with the real-time droop layer into a single closed loop. At each step, the time-coupled OPF uses the forecasted wind-speed trajectory to compute the baseline converter setpoints. In real-time operation, actual wind generation inevitably deviates from the forecast. The resulting power imbalance between the OPF-scheduled setpoints and the instantaneous operating point is dynamically compensated by the adaptive droop controller via the voltage and frequency adjustment terms in (20). The coordination among the forecasting, OPF, and droop layers is illustrated in Figure 2.

The computational flow within the proposed HIL control framework is illustrated in Figure 3. The Real-Time Digital Simulator (RTDS) exchanges real-time data with an external optimization framework based on PowerModelsACDC.jl developed in Julia [20], where the Interior Point OPTimizer (IPOPT) is employed to solve the OPF problem.

Specifically, RTDS transmits system measurements such as the active and reactive power demands (P_i^D, Q_i^D) to the Julia environment. The predicted wind speed is used to determine the wind farm generation (P_{WF}^G), which is included in the OPF formulation together with system parameters and operational constraints ($U_{i,min}$, $U_{i,max}$, $P_{i,max}^G$, ...). After executing the OPF, the computed results, including bus voltages, phase angles, power injections, and DC link voltages (U_i, δ_i, P_i, Q_i, $U_{dc,i}$), are retrieved to calculate updated setpoints ($U_{i,ref}^G$, $P_{i,ref}^G$, $P_{k,ref}^{VSC}$, $Q_{k,ref}^{VSC}$, $U_{k,ref}^{VSC}$, $U_{dc,k,ref}^{VSC}$). These setpoints are then communicated back to RTDS for real-time implementation.

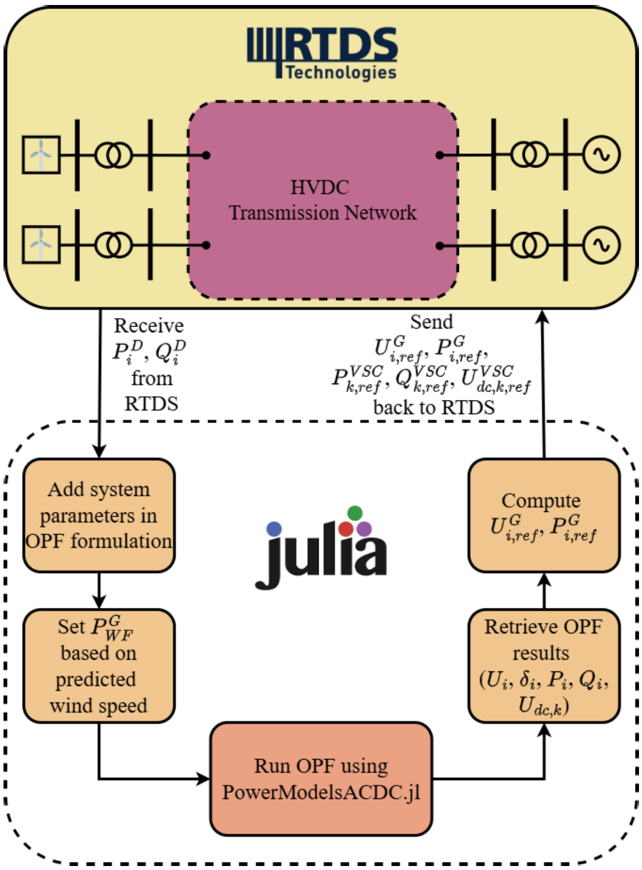

FIGURE 3. Computational flow within the HIL control framework.

The proposed framework scales efficiently to large-scale meshed AC–MTDC systems while meeting strict real-time requirements. First, the wind forecasting mechanism scales linearly with the number of wind farms. For macroscopic scheduling, the optimization routine employs a proven OPF formulation [20] that supports complex meshed DC topologies. It averages a 0.047 s solution time on the four-terminal benchmark and scales to transmission-size instances within minutes, comfortably accommodating the 30-minute update cadence. The scheduled setpoints are then transmitted to the RTDS via a GTNETx2 interface with a negligible 3 ms latency. Concurrently, the primary droop control executes entirely locally within the RTDS at a native 50 μs time step, eliminating peer-to-peer communication overhead. Furthermore, the margin-aware normalization in (23)–(24) dynamically adapts reserve allocations to the operating points, requiring no parameter re-tuning as wind penetration grows. However, extreme renewable penetration with critically low inertia would necessitate complementary grid-forming controls, which remains a focus for future work.

IV. SIMULATION RESULTS

To evaluate the proposed control framework, a meshed AC–MTDC system serves as the experimental testbed. Depicted in Figure 4, this configuration interconnects two IEEE 9-bus benchmark AC grids and two offshore wind farms through a 4-terminal DC network. Detailed system parameters, adapted from [26], are summarized in Table 2.

TABLE 2. Main parameters of the hybrid AC–MTDC test system.

System parameter	Onshore MMC	Offshore MMC
Rated converter power	2000 MVA	2000 MVA
Fundamental frequency	60 Hz	50 Hz
AC grid voltage	230 kV	220 kV
DC grid voltage (bipolar)	±525 kV	±525 kV
Transformer reactance	0.18 p.u.	0.15 p.u.
MMC arm inductance	0.05 mH	0.1 mH
MMC arm resistance	0.157 Ω	0.157 Ω
Submodule capacitance	25 mF	15 mF
Submodules per arm	220	220

To comprehensively evaluate system performance across diverse operating conditions, the proposed control strategy is benchmarked against conventional active power control, DC voltage control, and adaptive voltage droop control. For all control strategies, VSCs 2 and 3 operate in AC voltage and frequency (V–f) control mode, while the control modes applied to VSCs 1 and 4 are defined as follows:

1) **Active power control:** VSC 1 operates under active power control and VSC 4 under DC voltage control, without adaptive response to voltage or frequency fluctuations.
2) **DC voltage control:** VSC 1 operates under DC voltage control mode and VSC 4 under active power control, without adaptive response to voltage or frequency fluctuations.
3) **Adaptive voltage droop control:** VSC 1 and VSC 4 operate under voltage droop control, where the voltage droop gains (k_v) are dynamically updated according to system operating conditions.
4) **Proposed droop control:** VSC 1 and VSC 4 operate under proposed droop control, where the droop coefficients (k_v and k_f) are dynamically adjusted according to the system operating conditions.

The four configurations above vary VSCs 1 and 4 together rather than VSC 1 in isolation, for two structural reasons. First, in modes 1 and 2, the DC grid must contain at least one converter that closes the power balance and provides the DC voltage reference. With the offshore VSCs 2 and 3 held in V–f mode, this DC-slack responsibility necessarily falls on the onshore pair, so that configuring VSC 1 in active power control requires VSC 4 to operate in DC voltage control, and vice versa. Modes 1 and 2 therefore represent the same master–slave scheme with the master and slave roles of the onshore pair swapped. Second, in modes 3 and 4, distributed droop control is, by design, a scheme in which the DC-voltage regulation duty is shared across the onshore converters. If VSC 4 were instead held in a stiff DC-voltage mode while VSC 1 operated in droop, VSC 4 would clamp the DC-link

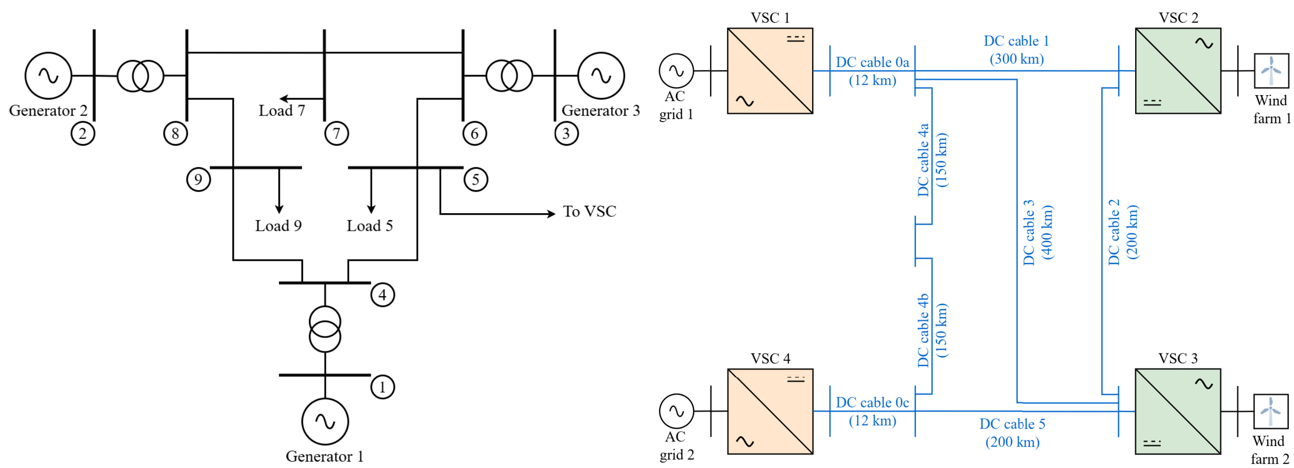

(a) IEEE 9 bus system (b) 4 terminal HVDC test system

FIGURE 4. Configuration of a 4-terminal AC–MTDC system where the AC grids 1 and 2 represent the IEEE 9 bus system.

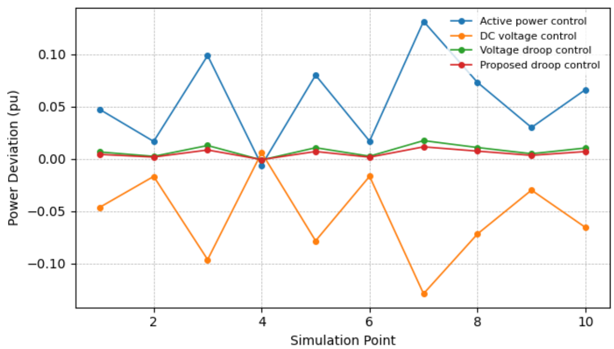

FIGURE 5. Power deviation at VSC 1.

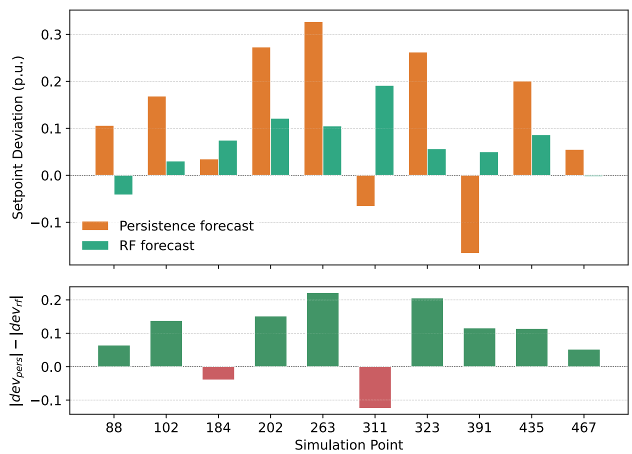

FIGURE 6. Active power setpoint deviation at VSC 1 in Scenario 1 under the RF and persistence forecasts, both measured against the perfect-foresight OPF. Per-point deviations at the top and the difference of absolute deviations at the bottom.

voltage near its reference and the deviation $U_{\mathrm{dc,ref}} - U_{\mathrm{dc,1}}$ seen by the droop term in (21) would be reduced to a near-zero residual, effectively suppressing the droop action and degenerating into a master–slave configuration. Modes 3 and 4, therefore, reconfigure both onshore stations to droop mode simultaneously. As a corollary of the role swap in modes 1 and 2, the VSC 1 response in one mode is the mirror image of its response in the other, so that only the performance of VSC 1 is reported to avoid redundancy.

Three representative scenarios are designed to evaluate the control strategies, reflecting realistic operating conditions and progressively increasing disturbance severity to assess control robustness.

1) **Scenario 1 – Normal condition:** The system operates under normal conditions while subjected to realistic wind forecast uncertainty in the two offshore wind farms.
2) **Scenario 2 – AC Step:** At $t = 1$ s, a sudden load increase of 500 MW is applied at bus 5 in the AC network connected to VSC 1.
3) **Scenario 3 – DC Fault:** At $t = 1$ s, a pole–to–pole DC fault occurs at the center of DC cable 1, followed by permanent disconnection of the affected line after fault clearance.

In Scenario 1, the active-power deviations of the four control strategies from the OPF reference at VSC 1 are shown in Figure 5. The proposed droop control yields the smallest deviations, followed by adaptive voltage droop control, while active power and DC voltage control exhibit the largest. This demonstrates that adaptive mechanisms responding jointly to voltage and frequency deviations effectively mitigate the impact of wind-forecast errors on converter power dispatch.

The preceding comparison fixed the forecast and varied the controller; the forecast itself, however, also shapes the OPF-scheduled setpoints. To isolate this second factor, two forecast configurations are compared under an identical downstream control structure: (i) the proposed RF forecast, and (ii) a 24-hour persistence baseline, in which the wind speed is assumed to equal the value observed 24 hours earlier, which is a standard day-ahead reference that exploits the diurnal periodicity of wind. For each simulation point, the resulting OPF setpoints are compared against those obtained under perfect foresight, where the OPF is fed the realized wind speed. Figure 6 reports the resulting setpoint deviations across ten simulation points randomly drawn from the test window. Under the RF forecast, the OPF setpoints achieve a substantially lower RMS deviation from the oracle values (0.092 p.u. at VSC 1) than under the persistence baseline (0.191 p.u., representing a factor of 2.08). This demonstrates that integrating predictive intelligence yields quantifiable advantages for OPF-based setpoint coordination, independent of any downstream dynamic control mechanisms.

These benefits can also be quantified in economic terms along two distinct dimensions. First, because steady-state setpoint deviations must be compensated via balancing-market dispatch, the 2.08-fold reduction in RMS deviation serves as a robust, model-independent proxy for balancing-energy savings under standard linear or piecewise-linear pricing frameworks. Second, evaluating the direct dispatch costs reveals that, averaged across the ten simulation points, the RF-driven approach reduces the mean generation cost by approximately 7.9% compared to the persistence-based baseline (a decrease in the OPF objective from roughly 4.78×10^5 to 4.40×10^5). Since both configurations utilize the identical OPF formulation, this cost differential explicitly isolates the economic value added by the forecast-integration step.

Figure 7 illustrates the dynamic response of VSC 1 under a 500 MW load increase in AC grid 1 at $t = 1$ s, with the corresponding quantitative indices summarized in Table 3. The disturbance originates on the AC side and produces only a negligible DC-voltage excursion at the converter terminals of the three voltage-only benchmarks ($\max|\Delta V_{\mathrm{dc}}| \leq 0.001$ p.u.). As a consequence, the DC-voltage deviation input that drives the adaptive voltage droop controller is approximately zero throughout the transient, and its active-power output reduces to that of a controller with a fixed reference. The three voltage-only benchmarks therefore degenerate into essentially equivalent active-power behavior in this scenario, as is visible from the close overlap of their trajectories in Figure 7(a) and (b). As shown in Figure 7(c), only DC voltage control returns the frequency to within the ± 0.5 % band by the end of the 10-second simulation window at $t_{s,f} \approx 7.7$ s, while active power and voltage droop control fail to recover. The three benchmarks provide negligible active-power frequency support ($\mathrm{RMS}|\Delta P| \leq 3 \times 10^{-4}$ p.u.). Consequently, the residual differences in their frequency recovery arise from the AC system's intrinsic dynamics rather than from converter action.

However, the proposed scheme responds differently. Through the frequency-aware adjustment term in (22), it actively increases the active-power injection into AC grid 1

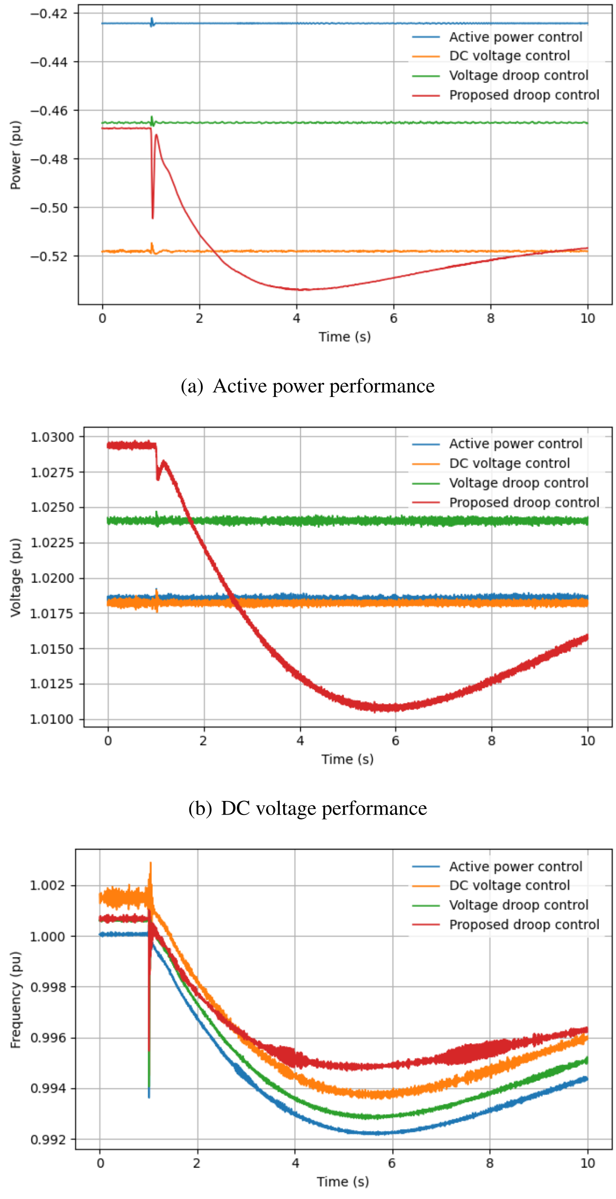

(a) Active power performance

(b) DC voltage performance

(c) Frequency performance

FIGURE 7. Dynamic responses of VSC 1 under different control strategies in Scenario 2.

in response to the frequency drop, thereby supporting frequency recovery. Because this additional active power is supplied from the DC side, the DC voltage at VSC 1 settles to a new steady-state value approximately 1.4 % below its pre-disturbance level, with a transient excursion of approximately 2 %. This trade-off is a direct manifestation of the voltage–frequency coupling that the proposed scheme is designed to exploit: the controller deliberately allocates a portion of the available DC-side margin to AC-frequency support, an action that the voltage-only benchmarks cannot perform by construction. As reported in Table 3, the proposed scheme reduces the maximum frequency deviation

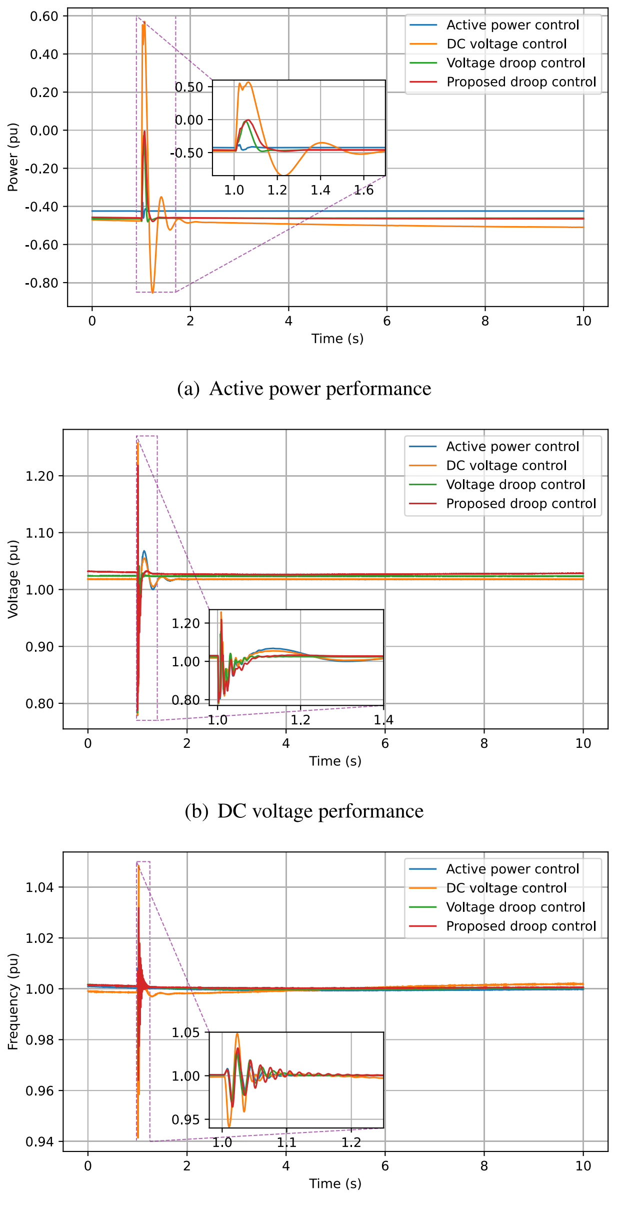

(a) Active power performance

(b) DC voltage performance

(c) Frequency performance

FIGURE 8. Dynamic responses of VSC 1 under different control strategies in Scenario 3.

by approximately 16 % relative to the best-performing benchmark and reduces the frequency integral absolute error (IAE) by approximately 11 %, and is the fastest controller to re-enter the ±0.5% frequency band (at $t_{s,f} \approx 6.8$ s). The accompanying DC-voltage offset remains well within the ±5 % operational band specified for VSC–MTDC systems, and the voltage trajectory exhibits no oscillatory or unstable behavior. These results confirm that the joint voltage–frequency coordination of the proposed scheme provides a structural capability in disturbance scenarios whose dominant response variable is AC frequency, at a moderate and predictable cost in DC-voltage regulation.

The dynamic behavior of VSC 1 under a severe DC network disturbance is evaluated in Scenario 3, as depicted in Figure 8. Specifically, a pole-to-pole fault strikes the midpoint of DC Cable 1 at $t = 1$ s and is subsequently cleared after a 5 ms breaker operating delay, permanently isolating the faulted line. The instantaneous DC voltage collapse during the fault is virtually identical across all four controllers, with the minimum DC voltage settling near 0.78 p.u. in every case. This is a direct consequence of network topology and cable impedance: during the sub-cycle following the short circuit, the voltage trajectory is dictated by the passive network response, and no converter controller is fast enough to alter the depth of the initial collapse. The discriminating performance among the four schemes, therefore, lies in the post-fault recovery phase rather than in the transient period.

In the recovery phase, voltage droop control achieves the fastest restoration of DC voltage to within ±2 % of its pre-disturbance value, requiring approximately 0.06 s, while the proposed scheme requires approximately 0.08 s. Both controllers recover the DC voltage roughly two to three times faster than the active power and DC voltage control benchmarks, whose post-fault settling times are approximately 0.20 s. This outcome is consistent with the design rationale of voltage droop control rather than indicative of a deficiency in the proposed scheme: a DC fault propagates primarily through the DC-voltage variable, so a droop law whose feedback signal is precisely the DC-voltage deviation is by construction near-optimally aligned with the recovery task in this disturbance class.

In terms of frequency regulation, voltage droop and active power control yield the smallest indices in this scenario, with the proposed scheme delivering closely comparable performance (frequency IAE of 2.5×10^{-3} p.u.·s, against 1.8×10^{-3} for voltage droop and 2.2×10^{-3} for active power), while DC voltage control performs markedly worse (5.9×10^{-3}, more than twice the others). The DC-voltage settling time of the proposed scheme exceeds that of voltage droop by approximately 0.02 s, which remains well within the post-fault recovery requirements of utility-grade AC–MTDC operation. The close correspondence with voltage droop on this DC-side disturbance class indicates that the joint voltage–frequency formulation does not compromise the DC-side disturbance handling capability, while additionally providing the AC-side regulation capability demonstrated in Scenario 2.

Taken together, Scenarios 2 and 3 indicate that active power control, DC voltage control, and adaptive voltage droop control are each structurally aligned with a specific disturbance class and exhibit substantially degraded performance outside it. Voltage droop control achieves the tightest DC-voltage recovery in Scenario 3 but degenerates into active-power behavior in Scenario 2. DC voltage control performs well on neither DC-side recovery of Scenario 3 nor on frequency regulation of Scenario 2 relative to the

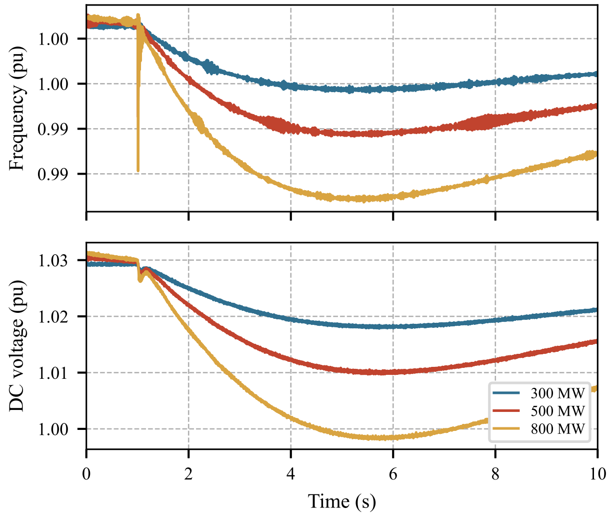

FIGURE 9. Dynamic response of VSC 1 under the proposed droop control for three AC-step magnitudes (300, 500, 800 MW) in Scenario 2.

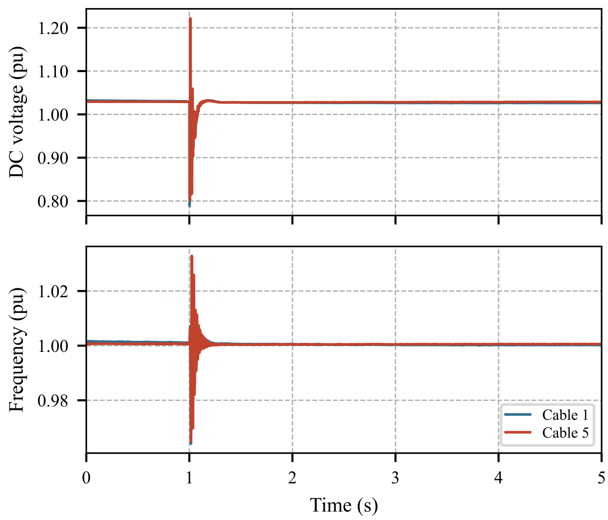

FIGURE 10. Dynamic response of VSC 1 under the proposed droop control for a pole-to-pole DC fault at the centre of Cable 1 (300 km) and of Cable 5 (200 km) in Scenario 3, with a common 5 ms breaker open duration.

other benchmarks. Futhermore, active power control provides no adaptive support in either scenario. The proposed scheme delivers consistent performance under both disturbance classes within a single controller: it attains the smallest maximum frequency deviation, the smallest frequency IAE, and the fastest re-entry into the $\pm 0.5\,\%$ frequency band in Scenario 2, and matches voltage droop control to within 0.02 s on DC-voltage settling in Scenario 3. No single benchmark achieves this combination of properties, which is precisely what low-inertia hybrid AC–MTDC systems with high renewable penetration require, since both AC- and DC-side disturbances are ideally managed by a unified control infrastructure.

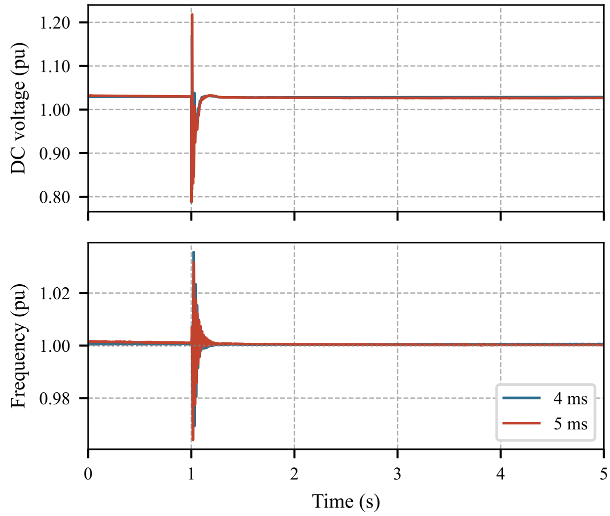

FIGURE 11. Effect of the fault-clearing (breaker open) duration on the proposed scheme for a Cable 1 DC fault for breaker open durations of 4 ms and 5 ms.

To assess robustness across the disturbance space, Table 3 extends the comparison to three AC-step magnitudes (300, 500, 800 MW) in Scenario 2, two fault locations (Cable 1, Cable 5) in Scenario 3 under a common 5 ms breaker open duration, and two breaker open durations (4 ms and 5 ms) on the Cable 1 fault. The proposed scheme's responses are shown in Figures 9, 10, and 11. As noted in Section III-B, the proposed scheme intentionally accepts a larger DC-voltage offset in order to tighten frequency regulation, so the indices in Table 3 should be read jointly rather than axis-by-axis.

As the AC-step magnitude increases, the proposed scheme consistently attains the smallest maximum frequency deviation and frequency IAE, with its advantage over the best benchmark widening from approximately 9% at 300 MW to 22% at 800 MW. Moreover, the associated DC-voltage offset grows by about 2.14% but remains within the converter's admissible range, consistent with the intended voltage–frequency trade-off.

To further investigate the impact of different fault locations, comparative simulations were conducted on both Cable 1 and Cable 5. As expected, the Cable 1 fault induces a deeper DC-voltage dip than the Cable 5 fault, which is consistent with its greater line length and its position on the main interconnecting branch. Despite this difference in severity, the proposed scheme behaves qualitatively the same at both locations: adaptive voltage droop control retains the tightest DC-voltage settling time (by design), while the proposed scheme delivers closely comparable DC-voltage recovery together with balanced frequency regulation.

In addition to fault locations, the robustness of the control framework against varying fault-clearing times was also evaluated. Comparing 4 ms and 5 ms breaker delays for the Cable 1 fault reveals nearly identical peak frequency deviations; the 5 ms case only incurs a modestly larger

TABLE 3. Quantitative dynamic-response indices at VSC 1 across disturbance magnitudes (Scenario 2), fault locations (Scenario 3), and fault-clearing durations (Scenario 3, cable 1). The proposed scheme uses $\alpha_v = 0.8$, $\alpha_f = 0.2$.

Scenario	Disturbance	Control mode	$\max\lvert\Delta V_{dc}\rvert$ (p.u.)	$\max\lvert\Delta f\rvert$ (p.u.)	$t_{s,V_{dc}}$ (s)	$t_{s,f}$ (s)	IAE_V (p.u.·s)	IAE_f (p.u.·s)	RMS$\lvert\Delta P\rvert$ (p.u.)
S2 (AC step)	300 MW	Active power	0.0004	0.0048	in band	in band	0.0008	0.0335	0.0001
		DC voltage	0.0006	0.0033	in band	in band	0.0008	0.0203	0.0002
		Voltage droop	0.0006	0.0041	in band	in band	0.0007	0.0274	0.0002
		Proposed	0.0114	0.0030	in band	in band	0.0781	0.0197	0.0338
	500 MW	Active power	0.0007	0.0079	in band	>9.0	0.0008	0.0550	0.0001
		DC voltage	0.0009	0.0064	in band	7.691	0.0007	0.0419	0.0002
		Voltage droop	0.0007	0.0072	in band	>9.0	0.0008	0.0493	0.0002
		Proposed	0.0203	0.0054	5.422	6.795	0.1409	0.0373	0.0576
	800 MW	Active power	0.0012	0.0131	in band	>9.0	0.0009	0.0913	0.0002
		DC voltage	0.0011	0.0117	in band	>9.0	0.0010	0.0773	0.0004
		Voltage droop	0.0011	0.0124	in band	>9.0	0.0009	0.0851	0.0003
		Proposed	0.0325	0.0091	>9.0	>9.0	0.2269	0.0634	0.0923
S3 (DC fault)	Cable 1	Active power	0.2396	0.0276	0.2080	0.0550	0.0155	0.0022	0.0036
		DC voltage	0.2393	0.0586	0.2000	0.0590	0.0109	0.0059	0.1597
		Voltage droop	0.2402	0.0304	0.0610	0.0810	0.0063	0.0018	0.0448
		Proposed (5 ms)	0.2428	0.0359	0.0810	0.1060	0.0234	0.0025	0.0567
		Proposed (4 ms)	0.2420	0.0356	0.0770	0.0890	0.0102	0.0031	0.0469
	Cable 5	Active power	0.2266	0.0220	0.1920	0.0620	0.0122	0.0007	0.0018
		DC voltage	0.2423	0.0581	0.2110	0.1270	0.0130	0.0058	0.1901
		Voltage droop	0.2267	0.0326	0.0680	0.0650	0.0065	0.0026	0.0477
		Proposed	0.2276	0.0351	0.0890	0.1050	0.0110	0.0031	0.0531

Settling band: $\pm 2\%$ for V_{dc} (referenced to the pre-disturbance value), $\pm 0.5\%$ for f (referenced to nominal).
"in band": deviation never leaves the band; ">9.0": does not re-enter the band within the simulation window.
IAE and RMS$\lvert\Delta P\rvert$ integration window: $[1, 10]$ s for Scenario 2, $[1, 5]$ s for Scenario 3. RMS$\lvert\Delta P\rvert$ is referenced to the pre-disturbance active power.
For Scenario 3, the breaker open duration is 5 ms unless otherwise noted. The Cable 1 vs. Cable 5 location comparison uses the common 5 ms duration.

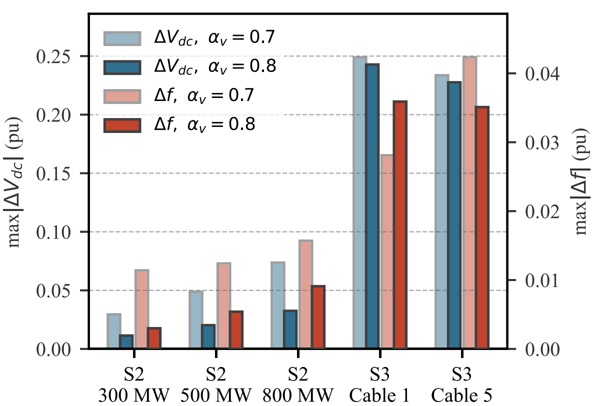

FIGURE 12. Peak dynamic indices of the proposed scheme at $\alpha_v = 0.7$and $\alpha_v = 0.8$ (with $\alpha_f = 1 - \alpha_v$) across the five disturbance cases: maximum DC-voltage deviation and maximum frequency deviation.

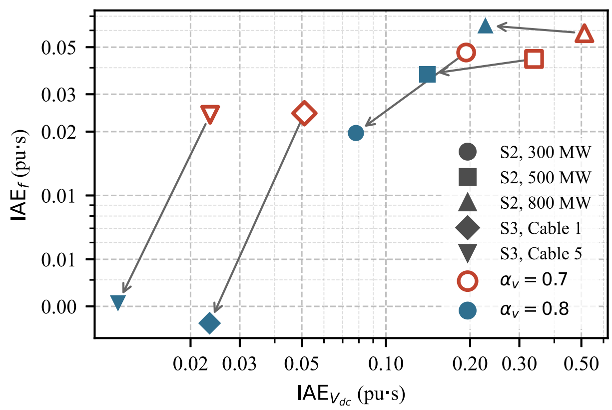

FIGURE 13. Trade-off between frequency and DC-voltage integral errors under the reserve-allocation parameter α_v. Each marker shape corresponds to one disturbance case; open markers denote $\alpha_v = 0.7$ and filled markers denote $\alpha_v = 0.8$. Grey arrows indicate the displacement from the lower to the higher allocation.

DC-voltage integral excursion, demonstrating the system's resilience to slight protection delays. The proposed scheme restores stable operation in both cases, confirming that its effectiveness is robust to the disturbance magnitude, location, and clearing duration considered.

The sensitivity of the proposed scheme to the reserve-allocation parameter α_v (with $\alpha_f = 1 - \alpha_v$) is reported in Figures 12 and 13, comparing $\alpha_v = 0.7$ and $\alpha_v = 0.8$ across all five disturbance cases. Both allocations yield bounded, stable responses in every case. The higher allocation $\alpha_v = 0.8$ adopted in the main results dominates the lower one on the integral and settling indices across all five cases. Specifically, the ($\mathrm{IAE}_{V_{dc}}$, IAE_f) plane in Figure 13 shows the operating point moving simultaneously toward the lower-left corner for most cases as α_v increases from 0.7 to 0.8, indicating joint improvement on both integral indices. This behavior is the empirical counterpart of the voltage–frequency coupling discussed in Section III-B: tighter DC-voltage regulation re-stabilizes the DC link more rapidly, which in turn relieves the frequency-regulation channel. Within the tested range, $\alpha_v = 0.8$ therefore offers the best joint damping and is adopted in the main results.

Evaluated across all three scenarios and on both regulatory axes, the proposed scheme provided the most balanced response among the four controllers, combining the fastest frequency recovery under AC-side disturbances with DC-fault recovery comparable to adaptive voltage droop, at a modest and predictable cost in DC-voltage offset.

V. CONCLUSION

This paper has presented an OPF-based adaptive control framework that integrates RF-based wind-speed forecasting with a joint DC-voltage and AC-frequency adaptive droop scheme for hybrid AC–MTDC systems with offshore wind farms. The forecasting module equips the time-coupled OPF with predictive wind profiles to derive the baseline converter setpoints. These setpoints are subsequently refined in real time by an adaptive droop controller, which dynamically scales its voltage and frequency adjustment terms based on the available converter power margin. HIL validations across wind-forecast uncertainties, AC-side load steps, and pole-to-pole DC faults demonstrate that the proposed scheme achieves the fastest frequency recovery under AC disturbances. Furthermore, it delivers DC-fault resilience comparable to adaptive voltage droop, incurring only a modest and predictable trade-off in DC-voltage offset.

The principal contribution is therefore best characterized as across-disturbance consistency rather than uniformly superior performance on any single axis. Adaptive voltage droop remains the appropriate choice when only DC-side disturbances are of concern, whereas the proposed scheme is justified when robust performance is required against both disturbance classes.

Future work will proceed in three directions: replacing the deterministic OPF with a stochastic or chance-constrained formulation that co-optimizes reserve against the wind distribution, internalizing at the scheduling layer the uncertainty presently handled only by the droop controller, and extending this to larger meshed AC–MTDC systems benchmarked against these baselines; benchmarking the RF forecaster against deep sequence models under a systematic sensitivity analysis of the history and prediction horizons (H, P) and the droop weights (α_v, α_f); and investigating decentralized reinforcement-learning-based droop tuning, benchmarked against model predictive control and coordinated secondary frequency control. Pursuing these directions will further establish the scalability and robustness of the proposed framework.

REFERENCES

[1] *Global Electricity Review 2025*, Ember, 2025.

[2] *Renewables 2024 Global Status Report Collection*, REN21, 2024.

[3] C.-K. Kim, V. K. Sood, G.-S. Jang, S.-J. Lim, and S.-J. Lee, *HVDC Transmission: Power Conversion Applications in Power Systems*. Hoboken, NJ, USA: Wiley, 2009.

[4] F. Muhammad, H. Rasheed, D. W. Spier, E. Prieto-Araujo, and O. G. Bellmunt, "Control design and fault handling performance of MMC for MMC-based DC distribution system," *IEEE Access*, vol. 10, pp. 126695–126711, 2022.

[5] A. Rabiee and A. Soroudi, "Stochastic multiperiod OPF model of power systems with HVDC-connected intermittent wind power generation," *IEEE Trans. Power Del.*, vol. 29, no. 1, pp. 336–344, Feb. 2014.

[6] Y. M. Atwa and E. F. El-Saadany, "Probabilistic approach for optimal allocation of wind-based distributed generation in distribution systems," *IET Renew. Power Gener.*, vol. 5, no. 1, pp. 79–88, Jan. 2011.

[7] L. A. Roald, D. Pozo, A. Papavasiliou, D. K. Molzahn, J. Kazempour, and A. Conejo, "Power systems optimization under uncertainty: A review of methods and applications," *Electr. Power Syst. Res.*, vol. 214, Jan. 2023, Art. no. 108725.

[8] A. Babiker, S. S. Ahmad, I. Ahmed, M. Khalid, M. A. Abido, and F. Saleh Al-Ismail, "Optimal power flow: A review of state-of-the-art techniques and future perspectives," *IEEE Access*, vol. 13, pp. 60012–60039, 2025.

[9] J. Beerten, D. V. Hertem, and R. J. M. Belmans, "VSC MTDC systems with a distributed DC voltage control—A power flow approach," in *Proc. IEEE Trondheim PowerTech*, Jun. 2011, pp. 1–6.

[10] J. Stojković, A. Lekić, and P. Stefanov, "Adaptive control of HVDC links for frequency stability enhancement in low-inertia systems," *Energies*, vol. 13, no. 23, p. 6162, Nov. 2020.

[11] Y. Wang, B. Li, Z. Zhou, Z. Chen, W. Wen, X. Li, and C. Wang, "DC voltage deviation-dependent voltage droop control method for VSC-MTDC systems under large disturbances," *IET Renew. Power Gener.*, vol. 14, no. 5, pp. 891–896, Apr. 2020.

[12] N. R. Chaudhuri and B. Chaudhuri, "Adaptive droop control for effective power sharing in multi-terminal DC (MTDC) grids," *IEEE Trans. Power Syst.*, vol. 28, no. 1, pp. 21–29, Feb. 2013.

[13] Y. Wang, W. Wen, C. Wang, H. Liu, X. Zhan, and X. Xiao, "Adaptive voltage droop method of multiterminal VSC-HVDC systems for DC voltage deviation and power sharing," *IEEE Trans. Power Del.*, vol. 34, no. 1, pp. 169–176, Feb. 2019.

[14] P. Prabhakaran, Y. Goyal, and V. Agarwal, "Novel nonlinear droop control techniques to overcome the load sharing and voltage regulation issues in DC microgrid," *IEEE Trans. Power Electron.*, vol. 33, no. 5, pp. 4477–4487, May 2018.

[15] V. T. K. Nguyen, Y.-K. Wu, and Q. D. Phan, "Adaptive droop control for compromise between DC voltage and frequency in multi-terminal HVDC," *IEEE Access*, vol. 9, pp. 131708–131719, 2021.

[16] J. Cao, W. Du, H. F. Wang, and S. Q. Bu, "Minimization of transmission loss in meshed AC/DC grids with VSC-MTDC networks," *IEEE Trans. Power Syst.*, vol. 28, no. 3, pp. 3047–3055, Aug. 2013.

[17] Y. Zhang, X. Meng, A. M. Shotorbani, and L. Wang, "Minimization of AC–DC grid transmission loss and DC voltage deviation using adaptive droop control and improved AC–DC power flow algorithm," *IEEE Trans. Power Syst.*, vol. 36, no. 1, pp. 744–756, Jan. 2021.

[18] J. Beerten, S. Cole, and R. Belmans, "A sequential AC/DC power flow algorithm for networks containing multi-terminal VSC HVDC systems," in *Proc. IEEE PES Gen. Meeting*, Jul. 2010, pp. 1–7.

[19] G. Daelemans, K. Srivastava, M. Reza, S. Cole, and R. Belmans, "Minimization of steady-state losses in meshed networks using VSC HVDC," in *Proc. IEEE Power Energy Soc. Gen. Meeting*, Jul. 2009, pp. 1–5.

[20] H. Ergun, J. Dave, D. Van Hertem, and F. Geth, "Optimal power flow for AC–DC grids: Formulation, convex relaxation, linear approximation, and implementation," *IEEE Trans. Power Syst.*, vol. 34, no. 4, pp. 2980–2990, Jul. 2019.

[21] K. Olcay, S. G. Tunca, and M. A. Özgür, "Forecasting and performance analysis of energy production in solar power plants using long short-term memory (LSTM) and random forest models," *IEEE Access*, vol. 12, pp. 103299–103312, 2024.

[22] Y. Wang, R. Zou, F. Liu, L. Zhang, and Q. Liu, "A review of wind speed and wind power forecasting with deep neural networks," *Appl. Energy*, vol. 304, Dec. 2021, Art. no. 117766.

[23] G. Iannace, G. Ciaburro, and A. Trematerra, "Wind turbine noise prediction using random forest regression," *Machines*, vol. 7, no. 4, p. 69, Nov. 2019.

[24] J. Browell, S. Haglund, H. Kälvegren, E. Simioni, R. Bessa, Y. Wang, and D. van der Meer, "Hybrid energy forecasting and trading competition," *IEEE DataPort*, 2024.

[25] A. Lahouar and J. Ben Hadj Slama, "Hour-ahead wind power forecast based on random forests," *Renew. Energy*, vol. 109, pp. 529–541, Aug. 2017.

[26] A. Shetgaonkar, T. Karmokar, M. Popov, and A. Lekić, "Enhanced real-time multiterminal HVDC power system benchmark models with performance evaluation strategies," *CIGRE Sci. Eng.*, vol. 32, pp. 1–29, Feb. 2024.

HONGJIN DU (Graduate Student Member, IEEE) received the B.Sc. and M.Sc. degrees in electrical engineering from Northeast Electric Power University (NEEPU), China, in 2015 and 2018, respectively. She is currently pursuing the Ph.D. degree with the Intelligent Electrical Power Grids (IEPG) Group, Delft University of Technology (TU Delft), The Netherlands. She was an Electrical Engineer at China Huadian Electric Power Research Institute (CHDER), from 2018 to 2022. Her primary research interests include coordinated optimal control for hybrid AC-MTDC power systems and power system analysis.

RAHUL RANE (Student Member, IEEE) received the B.Eng. degree in electrical engineering from Veermata Jijabai Technological Institute (VJTI), Mumbai, India, in 2021, and the M.Sc. degree in electrical engineering from Delft University of Technology, The Netherlands, in 2024, where he is currently pursuing the Ph.D. degree with the Intelligent Electrical Power Grids Group. His primary research interests include modeling, stability analysis, control, and the application of machine learning in power electronic-dominated power systems.

WEIJIE XIA (Student Member, IEEE) received the B.Sc. degree from the Ocean University of China, in 2018, and the dual M.Sc. degree in sustainable energy technology from KTH Royal Institute of Technology, Sweden, and Eindhoven University of Technology, The Netherlands, in 2022. He is currently pursuing the Ph.D. degree with the Intelligent Electrical Power Grids Group, Delft University of Technology, The Netherlands. His primary research interests include the interdisciplinary areas of machine learning and energy systems.

PEDRO P. VERGARA (Senior Member, IEEE) received the B.Sc. degree in electrical engineering from the Universidad Industrial de Santander (UIS), Colombia, the M.Sc. degree in electrical engineering from the University of Campinas (UNICAMP), Brazil, and the dual Ph.D. degree in electrical engineering from UNICAMP, and the University of Southern Denmark (SDU), Denmark.

His postdoctoral work was conducted with the Electrical Energy Systems Group, Eindhoven University of Technology (TU/e), The Netherlands. He is currently an Associate Professor with the Intelligent Electrical Power Grids Group, Delft University of Technology, The Netherlands.

ALEKSANDRA LEKIĆ (Senior Member, IEEE) received the B.S., M.S., and Ph.D. degrees in electrical engineering from the University of Belgrade, Serbia, in 2012, 2013, and 2017, respectively.

She was a Teaching Assistant and an Assistant Professor with the University of Belgrade, and a Postdoctoral Researcher at KU Leuven and EnergyVille, Belgium. From 2020 to 2025, she was an Assistant Professor at Delft University of Technology, where she is currently an Associate Professor. Her research interests include the control and stability of nonlinear switching converters, renewable-integrated hybrid power systems, HVDC systems, impedance-based harmonic stability for MMC models, and advanced control algorithms.